

Determination of primary electron spectra from incoherent scatter radar measurements of the auroral *E* region

Joshua Semeter¹

Department of Electrical and Computer Engineering and Center for Space Physics, Boston University, Boston, Massachusetts, USA

Farzad Kamalabadi

Department of Electrical and Computer Engineering, University of Illinois at Urbana-Champaign, Urbana, Illinois, USA

Received 6 February 2004; revised 2 November 2004; accepted 25 January 2005; published 15 April 2005.

[1] A technique is presented for inverting incoherent scatter radar (ISR) measurements of the auroral ionosphere to determine the incident electron energy spectrum. A linear model is constructed relating electron differential number flux to the volume production rate of ions, the latter derived from measured electron density profiles using a continuity equation. The forward model is inverted using the maximum entropy method (MEM). This implementation of ISR inversion was found to be remarkably robust to the principal sources of model and measurement uncertainty. The procedure was applied to high-resolution measurements ($1.2 \text{ s} \times 1 \text{ km}$) by the Sondrestrom ISR recorded during an auroral surge. Analysis of bulk plasma properties in the recovered spectra suggested that the relationship between the characteristic energy and the net number flux was highly nonlinear during the onset of the auroral surge, an observation that can now be evaluated statistically. This perspective on the temporal behavior of the auroral acceleration region cannot be accessed through spaceborne measurements; ISR inversion thus constitutes a critical tool for addressing time-dependent coupling of the magnetosphere and ionosphere.

Citation: Semeter, J., and F. Kamalabadi (2005), Determination of primary electron spectra from incoherent scatter radar measurements of the auroral *E* region, *Radio Sci.*, 40, RS2006, doi:10.1029/2004RS003042.

1. Introduction

[2] Measurements of photon and ion production in the aurora have long been used to infer information about the energy spectrum of the causative magnetospheric particle flux. Early quantitative analyses of this type involved passive optical measurements. *Rees and Luckey* [1974], for instance, used simultaneous measurements of the oxygen emission lines at 630 nm and 557.7 nm and the N_2^+ band emission sampled at 427.8 nm in electron aurora to parameterize the incident energy spectrum in terms of its characteristic energy and total energy flux. This approach was later extended to other wavelengths using first principles modeling [*Lummerzheim and Liliensten*, 1994; *Strickland et al.*, 1989; *Semeter et al.*,

2001a], allowing, for example, atmospheric composition factors to be included in the inversion [e.g., *Hecht et al.*, 1991; *Meier et al.*, 1989].

[3] With the advent of incoherent scatter radar (ISR) came the ability to remotely sense enhancements in plasma density produced by auroral precipitation. Measurements of the electron density profile through the auroral *E* region present an inverse problem with many degrees of freedom compared with optical measurements. Under assumptions that will be discussed at length in this paper, plasma density as a function of altitude and time can be inverted to determine the time-dependent energy spectrum of the incident particle flux with no prior assumption about its functional form. *Vondrak and Baron* [1975] implemented this technique as a sequential residual minimization problem under the name UNTANGLE. A drawback in their approach is that errors are multiplied at each step, such that the result is dependent on the order in which coefficients are found. *Brekke et al.* [1989] recast the problem in matrix form

¹Formerly at SRI International, Menlo Park, California, USA.

under the name CARD, which provided an improved framework for error analysis. A further refinement was implemented by *Kirkwood* [1988], who considered non-steady state conditions.

[4] Although ISR profile inversion has been used in geophysical studies by several authors [e.g., *Moen et al.*, 1990; *Kirkwood and Eliasson*, 1990a; *Burns et al.*, 1990; *Osepian and Kirkwood*, 1996], the reliability of the estimated spectra has never been addressed in any systematic way. *Kirkwood and Eliasson* [1990b] and *Osepian and Kirkwood* [1996] demonstrated order-of-magnitude agreement with near-conjugate satellite measurements of the incident spectrum, but it is equally important to evaluate the robustness of the procedure itself to various model assumptions and measurement uncertainties. In this paper we describe a variant implementation of the time-dependent ISR inversion technique that uses the Maximum Entropy Method (MEM), and investigate the sensitivity of the procedure to the principle sources of systematic and statistical uncertainty. Our results suggest that the limited spectral resolution achieved in prior ISR inversion results is not caused by intrinsic limitations in the technique, but is rather a consequence of the inversion algorithm applied. We also show that the bulk parameters in the recovered spectra (characteristic energy, energy flux, and number flux) are surprisingly insensitive to model assumptions.

[5] The overarching goal of this work is to establish the ground-based determination of primary auroral electron spectra as a critical tool for understanding the temporal development of the auroral acceleration region. The inversion of ground-based measurements is the only approach by which one can investigate the time-dependent behavior of the auroral acceleration region in the frame of reference of a developing auroral arc, and over timescales relevant to the physics of auroral formation (i.e., tens of seconds to a few minutes). This perspective cannot be accessed using satellite sensors, which cross a discrete arc in less than 1 s. Our focus is primarily on dynamic electron aurora, but the procedure is readily adaptable to proton precipitation using a modified forward model.

[6] Our presentation begins with a detailed description of the ISR inversion procedure. For our forward model we follow the semiempirical approach of *Rees* [1963], but use the improved laboratory measurements of *Cohn and Caledonia* [1970]. The resulting model kernel suggests the use of an edge-preserving inversion procedure such as Maximum Entropy. We demonstrate by example the efficacy with which MEM handles the intrinsic ill-conditioning of the ISR inversion problem. We then proceed to evaluate the robustness of the procedure to the three principal model uncertainties and the three principal measurement uncertainties using a representative auroral electron spectrum measured by the FAST

satellite and its computed ionospheric response. Of particular interest is the sensitivity of the characteristic energy and net number flux of the recovered distributions to these sources of error. Finally, we present a time-dependent inversion of an auroral surge recorded by the Sondrestrom IS radar. The results suggest a highly nonlinear relationship between characteristic energy and electron number flux during auroral formation.

2. ISR Inversion Procedure

[7] There are essentially three elements to the ISR inversion procedure. First, measurements of ion density are used in a continuity calculation to estimate the ion production rate q as a function of altitude. In the frame of reference of an auroral flux tube, continuity may be expressed as

$$\frac{dn}{dt} = q - \alpha n^2, \quad (1)$$

where n is ion density (the plasma is quasi-neutral, such that $n_e = n_i = n$), α is the effective recombination coefficient, and q is the ion production rate. Second, a numerical model is used to compute $q(z)$ for a discrete set of monoenergetic electron beams. The computed profiles constitute a discrete forward model A relating an arbitrary discretized incident number flux spectrum ϕ to a corresponding altitude profile of ion production, i.e., $\mathbf{q} = \mathbf{A}\phi$. Last, ϕ is estimated via inversion of matrix \mathbf{A} to arrive a discrete estimate of the differential number flux spectrum.

[8] Section 2.1 describes our implementation of this procedure in detail, with due justification of the assumptions involved and with due attention to error propagation. Although some of this development has been published elsewhere, our methodology diverges from prior implementations of ISR inversion in several key respects, and so the complete formulation of the model is presented. MKS units are used throughout (except in our use of eV for energy, which remains standard in space plasma physics).

2.1. Forward Model

[9] Computing the ionization profile for a given pitch angle distribution of impinging auroral electrons has been addressed by several authors using one of two basic approaches. One approach computes ionization from first principles by solving the electron transport equation [*Strickland et al.*, 1989; *Lummerzheim and Liliensten*, 1994], and the other makes use of laboratory measurements of the distribution of optical energy produced by the attenuation of an electron beam fired into an air filled chamber [*Grün and Barth*, 1957; *Cohn and Caledonia*, 1970; *Barrett and Hays*, 1976]. In the latter

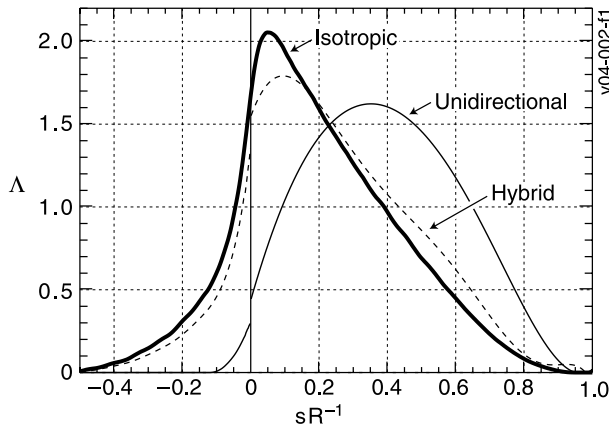


Figure 1. Universal energy dissipation functions computed from the laboratory measurements of *Cohn and Caledonia* [1970] for three assumed pitch angle distributions.

approach, all relevant physics is included implicitly in the experiments, and the results are conveniently expressed in terms of a universal energy deposition curve which is easily extrapolated to ionospheric densities and distances [Rees, 1963]. We use this approach here because it is easily adapted to linear inverse theory.

[10] For initial energies $K > 300$ eV, *Barrett and Hays* [1976] found that the range of an electron in air is well represented by the empirical formula

$$R = 4.3 + 53.6K^{1.67} - 0.038K^{-0.7} [\text{kg m}^{-2}] \quad (2)$$

where R is in units of mass distance. The scattering depth at distance z projected along the magnetic field can be also be specified in units of mass distance,

$$s = \sec(I) \int_z^\infty \rho(z) dz \quad [\text{kg m}^{-2}] \quad (3)$$

where I is the magnetic inclination and ρ is the atmospheric mass density computed, for instance, using a model such as the Mass Spectrometer and Incoherent Scatter (MSIS) model [Hedin, 1991]. We assume $I = 0^\circ$ (vertical field lines) for the remainder of this paper. (The inclination at Sondrestrom, Greenland, is 11° , which constitutes a negligible correction to our results.)

[11] For $K > 1$ keV, the rate of energy dissipation as a function of normalized distance s/R has been found to be independent of K . We may, therefore, define a universal energy dissipation function, Λ , as the fraction of the initial energy lost per fraction of mass distance travelled, i.e.,

$$\Lambda \equiv \frac{dE/K}{ds/R} \quad (4)$$

with the normalization $\int_{-1}^{+1} \Lambda(s/R) d(s/R) = 1$ imposed by conservation of energy.

[12] Several authors have computed Λ for a unidirectional beam of electrons [Rees, 1963; Cohn and Caledonia, 1970; Barrett and Hays, 1976]. Although the agreement is generally good, there is some discrepancy for small values of $|s/R|$. Figure 1 shows Λ for three assumed pitch angle distribution, using the isophote contours of *Cohn and Caledonia* [1970]. The curve labelled “unidirectional” differs somewhat from the unidirectional curve of [Rees, 1963], which was computed from the earlier measurements of *Grün and Barth* [1957]. The discrepancy at small values of $|s/R|$ can be attributed to differences in the experimental apparatus used by *Grün and Barth* [1957] and *Cohn and Caledonia* [1970]; specifically, it is likely that the backscattered energy was more accurately accounted for by *Cohn and Caledonia*. Indeed, the sharp discontinuity at $s/R = 0$ in the *Rees* [1963] result has no physical basis. This discontinuity is reduced in our result.

[13] The unidirectional Λ in Figure 1 corresponds to an auroral electron flux that is confined to the downward field-aligned direction. However, measurements show that auroral primaries are distributed broadly within the $\pm 90^\circ$ ionospheric source cone. The curve labelled “isotropic” in Figure 1 was computed for a uniform distribution of electrons in the downward hemisphere via appropriate rotations and summations over the *Cohn and Caledonia* [1970] isophotes. Compared with the unidirectional curve, much more of the total energy is deposited at smaller values of s/R , corresponding to higher altitudes, and 18% of the incident energy is now lost as backscatter to the magnetosphere.

[14] Observed pitch angle distributions for >1 keV electron precipitation are typically isotropic but with a peak in the downward field-aligned direction. *Semeter et al.* [2001b, Figure 3] presented several pitch angle distributions measured over active aurora by the PHAZE2 sounding rocket. The downward peak is typically a factor of ~ 10 greater than the isotropic density and is confined to $\pm 10^\circ$ of the downward direction. In Figure 1, the curve labeled “hybrid” was computed for an isotropic distribution but with a factor 10 increase within a $\pm 10^\circ$ cone in the downward direction. The result differs only mildly from the isotropic curve. This means that despite the enhancement in field-aligned flux, the majority of the flux is still carried by the isotropic population.

[15] The actual Λ is probably even closer to the isotropic curve for the following reason. Referring again to *Semeter et al.* [2001b, Figure 3], the field-aligned enhancement invariably cuts off above a few keV. Most of the energy flux is thus carried by the highest energy electrons, and these tend to have a strictly isotropic source cone distribution. We conclude that the isotropic

Table 1. Λ for Isotropic Pitch Angle Distribution

s/R	Λ	s/R	Λ	s/R	Λ
-0.525	0.000	-0.025	1.237	0.475	0.759
-0.500	0.006	0.000	1.686	0.500	0.689
-0.475	0.020	0.025	1.995	0.525	0.636
-0.450	0.027	0.050	2.063	0.550	0.567
-0.425	0.042	0.075	2.024	0.575	0.504
-0.400	0.058	0.100	1.946	0.600	0.450
-0.375	0.069	0.125	1.846	0.625	0.388
-0.350	0.091	0.150	1.761	0.650	0.334
-0.325	0.123	0.175	1.681	0.675	0.282
-0.300	0.145	0.200	1.596	0.700	0.231
-0.275	0.181	0.225	1.502	0.725	0.187
-0.250	0.214	0.250	1.421	0.750	0.149
-0.225	0.248	0.275	1.346	0.775	0.113
-0.200	0.313	0.300	1.260	0.800	0.081
-0.175	0.360	0.325	1.190	0.825	0.058
-0.150	0.431	0.350	1.101	0.850	0.037
-0.125	0.499	0.375	1.043	0.875	0.023
-0.100	0.604	0.400	0.972	0.900	0.010
-0.075	0.728	0.425	0.888	0.925	0.002
-0.050	0.934	0.450	0.834	0.950	0.000

curve in Figure 1 constitutes the most accurate model of dynamic aurora. Table 1 gives tabulated values for this curve.

[16] The results of Figure 1 are scaled to auroral distances by substituting $ds = \rho dz$ from (3) into (4) to give

$$\frac{dE}{dz} = \frac{\Lambda \rho K}{R}. \quad [\text{eV m}^{-1}] \quad (5)$$

Equation (5) describes the change in energy versus altitude for a single electron directed downward at the top of the atmosphere. Consider now a flux F of electrons all with initial kinetic energy K impacting a differential surface da which is orthogonal to dz . The total number of electrons entering a differential volume element $dV = dadz$ is $F \cdot da$ [Vallance-Jones, 1974]. Equation (5) can thus be written

$$\varepsilon(z, K) \equiv \frac{dE}{dV} = \frac{\Lambda \rho KF}{R} \quad [\text{eV m}^{-3} \text{s}^{-1}]. \quad (6)$$

Equation (6) gives the rate of energy loss per unit volume as a function of altitude and initial energy.

[17] A well known empirical result is that the average energy lost per electron-ion pair produced is ~ 35.5 eV. For $K > 100$ eV, this value does not depend on the initial energy of the impinging electron or on the atmospheric composition [Fano, 1946; Dalgarno, 1962]. Dividing (6) by 35.5 gives the volume production rate of ions as a function of altitude for a flux F of electrons with energy K

$$q(z, K) = \frac{\Lambda \rho KF}{35.5R}. \quad [\text{m}^{-3} \text{s}^{-1}] \quad (7)$$

Figure 2 plots $q(z)$ for various values of K for typical nighttime polar atmosphere and an incident flux of $F = 1 \times 10^{12} \text{ m}^{-2} \text{ s}^{-1}$. These curves may be compared with Rees [1989, Figure 3.3.3]; for reasons discussed earlier, our model places the peak ionization at a somewhat higher altitude.

[18] Equation (7) can be used to construct a linear discrete model by which $q(z)$ can be computed for an arbitrary incident energy distribution. Consider a differential flux dF distributed uniformly over energy range K to $K + dK$ such that $dF = \phi(K)dK$. The total production rate at altitude z is given by

$$q(z) = \int_{K_{\min}}^{K_{\max}} \left[\frac{\Lambda \left(\frac{s(z)}{R(K)} \right) \rho(z) K}{35.5R(K)} \right] \phi(K) dK \quad [\text{m}^{-3} \text{s}^{-1}] \quad (8)$$

where the functional dependencies are now shown explicitly. The function $\phi(K)$ is the differential number flux integrated over pitch angle in the downward hemisphere with units of $\text{m}^{-2} \text{ s}^{-1} \text{ eV}^{-1}$. This parameter is commonly derived from rocketborne or satelliteborne measurements made, for instance, by an electrostatic analyzer. Note that we now recover the monoenergetic curves of Figure 2 by letting $\phi(K) = 1 \times 10^{12} \delta(K - K_0)$, where δ is the dirac delta function and K_0 is the beam energy.

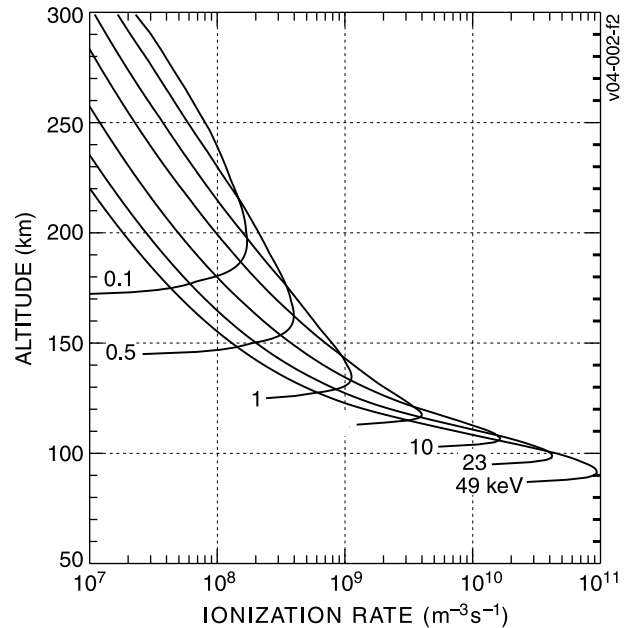


Figure 2. Ion production rate produced in the attenuation of a monoenergetic flux of $10^{12} \text{ m}^{-2} \text{ s}^{-1}$ with initial energy as given.

[19] Mathematically, (8) represents a Friedholm integral equation of the first kind, that is,

$$q(z) = \int_{K_{\min}}^{K_{\max}} A(z, K) \phi(K) dK \quad (9)$$

with A given by the bracketed expression in (8). Our goal is to solve for the unknown function $\phi(K)$ given $q(z)$ and $A(z, K)$. To accomplish this, we expand $\phi(K)$ into a discrete set of basis functions $\psi_j(K)$, i.e.,

$$\phi(K) = \sum_{j=1}^J \phi_j \psi_j(K). \quad (10)$$

The total production rate at altitude z can then be represented as:

$$q(z) = \int_{K_{\min}}^{K_{\max}} A(z, K) \sum_{j=1}^J \phi_j \psi_j(K) dK \quad (11)$$

or equivalently as:

$$q(z) = \sum_{j=1}^J \left[\int_{K_{\min}}^{K_{\max}} A(z, K) \psi_j(K) dK \right] \phi_j. \quad (12)$$

The choice of the basis function is generally guided by the attributes of the particular inverse problem at hand. The use of orthogonal rectangular functions,

$$\psi_j(K) = \begin{cases} 1 & K_{j-1} < K < K_j \\ 0 & \text{otherwise} \end{cases} \quad (13)$$

leads to:

$$q(z) = \sum_{j=1}^J A(z, K_j) \Delta K_j \phi_j \quad (14)$$

where $\Delta K_j = K_j - K_{j-1}$ is the width of the j th energy bin. This basis preserves the physical interpretation of ϕ_j as a discrete estimate of the differential number flux at energy K_j .

[20] Although this basis has been universally applied to the ISR inversion problem, it is by no means the only basis, or even the optimal basis, for the problem. For instance, if $\phi(K)$ is known a priori to have a single monoenergetic peak, one may wish to expand $\phi(K)$ in a basis which enforces this property; for instance, a Gaussian or drifting Maxwellian function could be used. In these cases, however, the inverse problem becomes nonlinear, requiring the use of optimization techniques to determine the ϕ_j [e.g., Semeter et al. 1999]. For this work we use the rectangular basis defined by (13).

[21] The ISR measurement process is inherently discrete due to the intrinsic height resolution of the

instrument. We may, therefore, discretize $q(z)$ by simple collocation. Equation (14) then becomes:

$$q(z_i) = \sum_{j=1}^J A(z_i, K_j) \Delta K_j \phi_j \quad (15)$$

or an equivalent matrix representation

$$\mathbf{q} = \mathbf{A} \phi \quad (16)$$

where \mathbf{A} has elements

$$A_{ij} = A(z_i, K_j) \Delta K_j = \frac{\Lambda \left(\frac{s(z_i)}{R(K_j)} \right) \rho(z_i) K_j \Delta K_j}{35.5 R(K_j)}. \quad (17)$$

Our discrete estimate of ϕ is computed via inversion of \mathbf{A} . What remains is to derive a suitable estimate of \mathbf{q} .

2.2. Estimating \mathbf{q}

[22] As stated in the introduction, there are two approaches one could take to estimate ion production rate from ground-based measurements. One approach involves photometric measurements of auroral luminosity, which provide a direct measure of ϵ in (6) integrated along the photometer line of sight [e.g., Christensen et al., 1987]. However, to derive $q(z)$ from such measurements requires the application of tomographic techniques using data from multiple locations. Such experiments have been performed [Frey et al., 1996; Gustavsson, 1998; Semeter et al., 1999; Kamalabadi et al., 2002] but the results have yet to be applied to the problem of estimating the full electron differential number flux spectrum.

[23] The second approach relies on analyzing ISR measurements of E region plasma density. In this approach, altitude information is acquired directly. However, ion density provides only an indirect measure of auroral energy deposition. One must invoke a continuity equation to derive $q(z)$ from measurements of $n(z)$. From (1) we have

$$q = \alpha n^2 + \frac{dn}{dt}. \quad (18)$$

[24] Equation (18) is nonlinear in n ; the response time of n to a change in q depends on its current value with time constant $\tau = 1/\alpha n$. A typical assumption is to ignore time variability and set $q = \alpha n^2$ (steady state), but it is important to understand where this assumption is valid. Figure 3 shows isocontours of $1/\alpha n$ as a function of n and altitude assuming a purely NO^+ ionosphere. A typical visible arc produces a density of $\sim 10^{12} \text{ m}^{-3}$ at ~ 110 km. Under such conditions, the dn/dt term in (18) can be neglected provided the impinging electron source does not vary over timescales shorter than a few seconds.

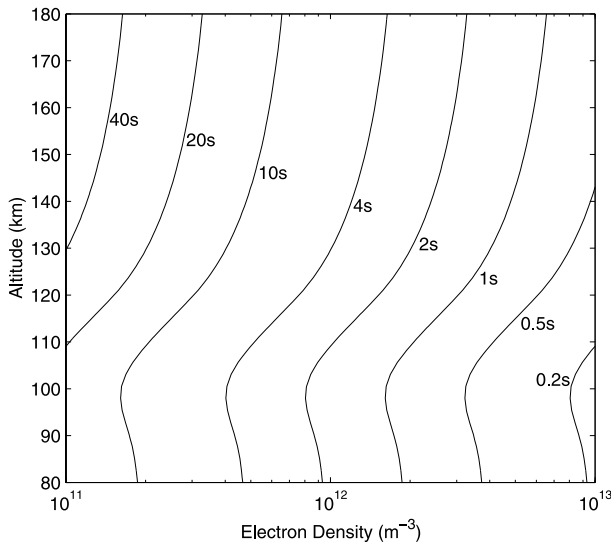


Figure 3. Isocontours of the ion recombination time constant $\tau = 1/\alpha n$ as function of plasma density and altitude.

However, when the plasma density is below $\sim 10^{11} \text{ m}^{-3}$ the response time of the ionosphere, either to a turn-on or a turn-off of the aurora, can be 10s of seconds. Such conditions might be expected, for example, just prior to substorm onset, or the onset of an auroral surge. Such a case where knowledge of dn/dt is important is presented in section 4.

[25] A further complication arises in that radar measurements are in an Earth-fixed reference frame. The time derivative of n computed from ISR measurements is, therefore, a convective derivative $Dn/Dt = dn/dt + \mathbf{v} \cdot \nabla n$, where \mathbf{v} is the horizontal plasma velocity relative to the Earth-fixed frame. If a flux tube supporting an auroral arc advects through the radar line of sight, Dn/Dt can be large even if the flux tube itself is in steady state.

[26] This ambiguity is best addressed using collocated optical measurements. Auroral imagery can be used to determine whether a nonzero Dn/Dt is caused by advection of an auroral flux tube (i.e., auroral motion through the radar volume), or true temporal variability in the auroral particle source. In section 4, high speed imagery was applied in this way.

2.3. Maximum Entropy Inversion

[27] Combining equations (9) and (18), the ISR inversion problem may be written as

$$\phi = \mathbf{A}^{inv} \left(\frac{d}{dt} \mathbf{n} + \alpha \mathbf{n}^2 \right). \quad (19)$$

The inverse problem is, in general, ill-posed since we may have a different number of measurements and

unknowns. Therefore \mathbf{A}^{inv} represents a satisfactorily close approximation to an inverse operation. The discretization of n is largely specified by the measurement resolution. With 1 km sampling through the E region, the vector \mathbf{n} will have ~ 50 elements. Our implementation of the derivative operator uses three-point Lagrangian interpolation. A simple two-point difference would give better time resolution and could be a better choice if the signal-to-noise ratio is high.

[28] We must next choose a discretization of ϕ . Intuition suggests that we formulate an overdetermined problem, i.e., fewer energy bins than altitude bins. However, we also wish to estimate the energy where the flux maximized (related to the parallel potential drop experienced by the electrons [Lyons *et al.*, 1979]) with high resolution. The question becomes how many samples of ϕ can we reliably recover in this basis, and how should these samples be distributed in energy?

[29] There are statistical and information-theoretic measures by which an optimal discretization can be chosen [e.g., Sharif and Kamalabadi 2004]. However, for our present purposes we focus, instead, on the empirical characteristics of our inverse problem and what they suggest in terms of an appropriate parameterization. Specifically, let us examine the nature of our discrete model \mathbf{A} . Figure 4 shows an image of $\log_{10}(\mathbf{A})$ computed for 55 logarithmically spaced energy bins in the interval 0.5 and 30 keV. Figure 4 is essentially a matrix representation of Figure 2. Clearly \mathbf{A} has significant off-diagonal elements and is, therefore, ill-conditioned in a mathematical sense. Thus we immediately see that a

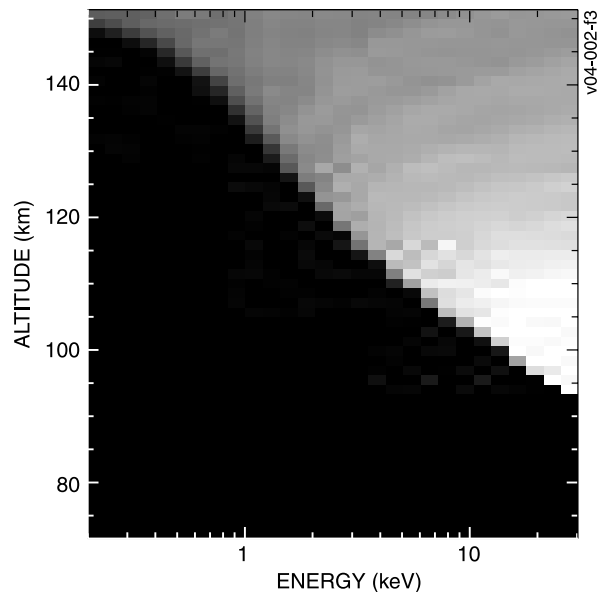


Figure 4. Image of $\log_{10}(\mathbf{A})$.

unique solution to the ISR inversion procedure is not guaranteed if noise is present in our measurements. However, \mathbf{A} does have properties that suggest an appropriate strategy to regularize the inversion. For large energies the columns of \mathbf{A} are characterized by an intense, sharp, peak at a low altitude, and for lower energies the peak is fainter and the ionization is more broadly distributed in altitude. A general class of inversion techniques that are especially suited for inverse problems exhibiting such a dichotomy exist under the general classification of nonquadratic regularization techniques. These techniques permit localized steep gradients in the reconstruction so that the edges are preserved. An example is the Total Variation regularization which had been applied to space-based tomographic studies by *Kamalabadi et al.* [2002]. Here, we employ another nonquadratic regularization technique, namely the maximum entropy inversion [*Censor, 1981*].

[30] The entropy of positive-valued discrete function may be defined as

$$-\sum_{j=1}^J \phi_j \log(\phi_j) \quad (20)$$

and can be interpreted as a measure of the uncertainty in the unknown. This view results from information theory where the unknown is normalized so that $\sum_{j=1}^J \phi_j = 1$, and may therefore be interpreted as a probability density function. As such, the maximum entropy solution may be viewed as the most noncommittal approach with respect to the unavailable information.

[31] The Maximum Entropy Method (MEM) has been widely used in astronomical image reconstruction [*Gull and Daniell, 1978*] for images which contain a mixture of bright point-like sources and extended, low-intensity sources. Experience has shown that MEM produces substantial energy concentration, resulting in sharp reconstruction of point objects. Our specific implementation of MEM maximizes the Berg entropy $-\sum_{j=1}^J \log(\phi_j)$ [*De Pierro, 1991*], and is a variant of the MEM application used in the auroral tomography work of *Semeter et al.* [1999]. This formulation leads to a nonlinear optimization problem that must be solved iteratively. The iteration steps are given in Appendix A.

[32] As a consequence of the nonorthogonality of \mathbf{A} and the parametric nature of the MEM inversion, the manner in which the energy bins are distributed is not critical. We have tested the inversion procedure for a variety of linear and nonlinear energy distributions and the results are virtually indistinguishable. The inversion even performs well when a mildly underdetermined problem is posed.

[33] Before proceeding to a detailed sensitivity analysis, we first demonstrate the effectiveness of MEM in

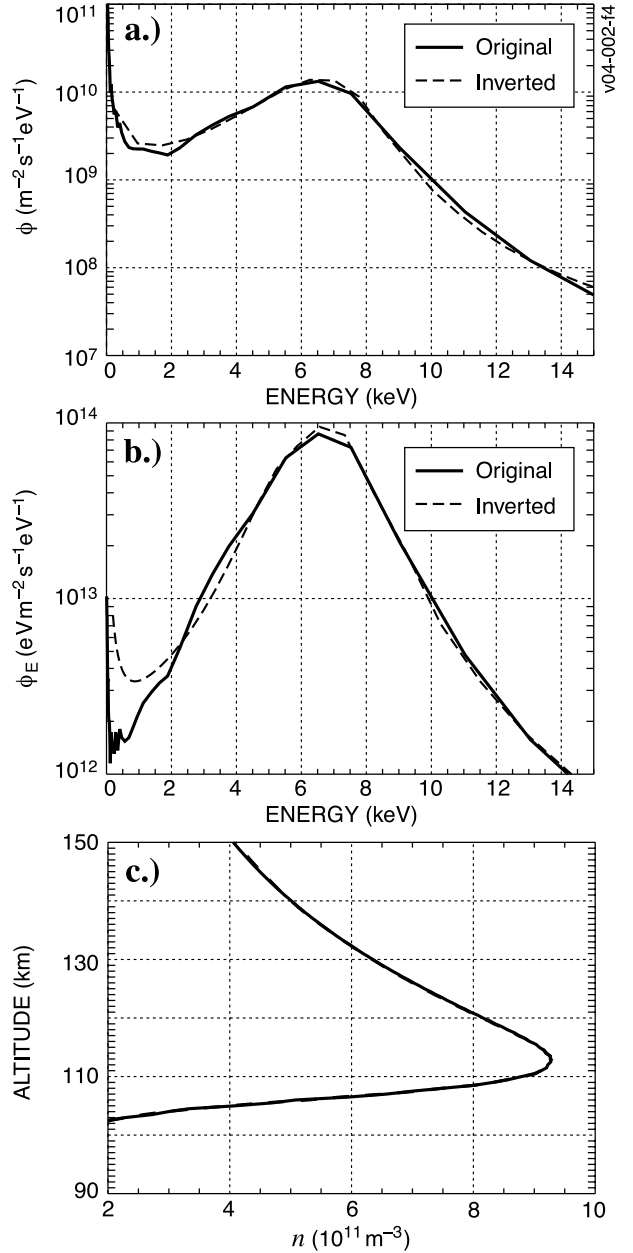


Figure 5. (a) Differential number flux ϕ of downgoing electrons measured by ESA instrument on the FAST satellite (solid) and recovered by ISR inversion (dashed). (b) Differential energy flux ϕ_E , measured (solid) and recovered (dashed). (c) Electron density enhancement computed from forward model.

handling the ill-conditioned nature of the ISR inversion problem using a known energy spectrum and its computed steady state density profile. Figure 5a (solid line) gives the electron differential number flux spectrum

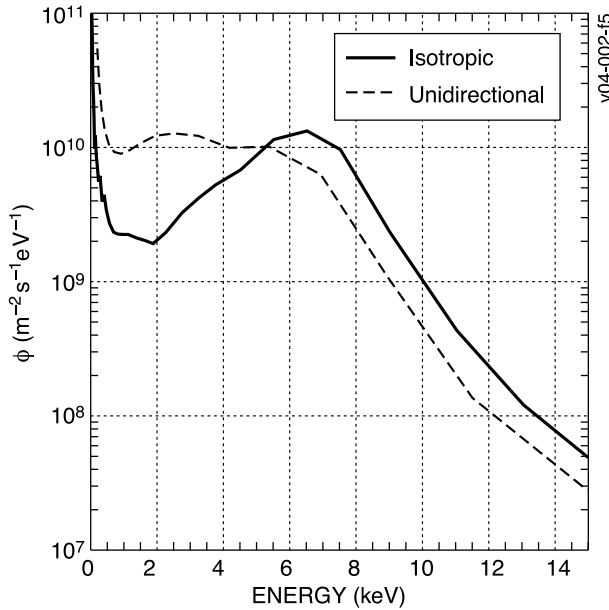


Figure 6. Effect of the pitch angle assumption on ISR inversion. The solid line is the measured ϕ ; the dashed line is the estimated ϕ when the incorrect pitch angle distribution (i.e., the unidirectional Λ) is applied in the inversion.

measured by the ESA instrument on the FAST satellite for 20 November 2001, 0147 UT (orbit 20876) integrated over all pitch angles in the downward hemisphere. This is representative of a typical “bump-on-tail” distribution over moderately active aurora. Figure 5b (solid line) presents the same data plotted as differential energy flux. Both forms of the energy spectrum are commonly found in the literature (see *Semeter et al.* [2001a] for further discussion of differences in interpretation). In this paper we focus primarily on the differential number flux spectrum ϕ .

[34] Figure 5c (solid line) gives the corresponding ionospheric profile computed using equations (8) and (18) (assuming $dn/dt = 0$). We have used the “isotropic” Λ tabulated in Table 1 and the MSISE-90 neutral atmosphere model [*Hedin*, 1991] to compute ρ . For the recombination rate, we assumed a purely NO^+ ionosphere and used the laboratory results of *Walls and Dunn* [1974]: $\alpha_{NO^+} = 4.2 \times 10^{-13} (300/Tn) \cdot 85 \text{ m}^3 \text{ s}^{-1}$.

[35] The dashed lines in Figures 5a and 5b give the recovered ϕ after the inversion of Figure 5c using the kernel shown in Figure 4. The algorithm was seeded with a uniform initial guess of $\phi = 1 \times 10^{13} \text{ m}^{-2} \text{ s}^{-1}$. A near perfect representation of ϕ was achieved for a wide range of initial guesses. We now use the number flux spectrum and computed density profile of Figure 5 to evaluate the

robustness of the inversion procedure to the principle sources of uncertainty.

3. Sources of Uncertainty

[36] In addition to issues concerning dn/dt discussed in section 2.2, there are six principle sources of uncertainty in the ISR inversion procedure: (1) the pitch angle distribution, (2) the recombination coefficient, (3) the neutral atmosphere model, (4) radar “pulse smearing” effects, (5) statistical errors in n , and (6) the use of range-corrected power as a measure of n . The first three are model uncertainties and the last three are measurement uncertainties. In considering the robustness of the inversion procedure to these uncertainties, one should bear in mind the following. What is of prime interest insofar as magnetospheric coupling is concerned is not the detailed shape of the recovered spectra, but rather the bulk properties of the spectra. Specifically, we wish to obtain a time-dependent estimate of the net number flux Φ , net energy flux Φ_E , and the characteristic energy (i.e., the location of the suprathermal peak) E_0 of the auroral source. These quantities are computed from the recovered spectra as follows:

$$\Phi = \sum_{j=0}^J \phi_j \Delta K_j \quad [\text{m}^{-2} \text{s}^{-1}] \quad (21)$$

$$\Phi_E = \sum_{j=0}^J \phi_j K_j \Delta K_j \quad [\text{eV m}^{-2} \text{s}^{-1}] \quad (22)$$

$$E_0 = \underset{K_j}{\text{argmax}} \{ \phi_E(K_j) \mid K_j > 500 \} \quad [\text{eV}] \quad (23)$$

$$E_{\text{avg}} = \Phi_E / \Phi \quad [\text{eV}] \quad (24)$$

E_0 represents the location of the “bump on tail” in the suprathermal (i.e., accelerated) electron population, often referred to as the characteristic energy for such distributions. In discussing bulk properties of auroral electron distributions, the average energy E_{avg} is also commonly used. The two parameters are often nearly equal. However, E_0 is the more relevant quantity for describing the auroral acceleration region (AAR) as it provides an estimate of the parallel energy gained by the distribution in the acceleration process and, hence, is proportional to the parallel drop in potential through the AAR. All of the recovered spectra we consider show clear evidence of such a parallel acceleration process.

3.1. Pitch Angle Distribution

[37] Figure 5c was computed using the isotropic curve from Figure 1. Figure 6 demonstrates what happens if the

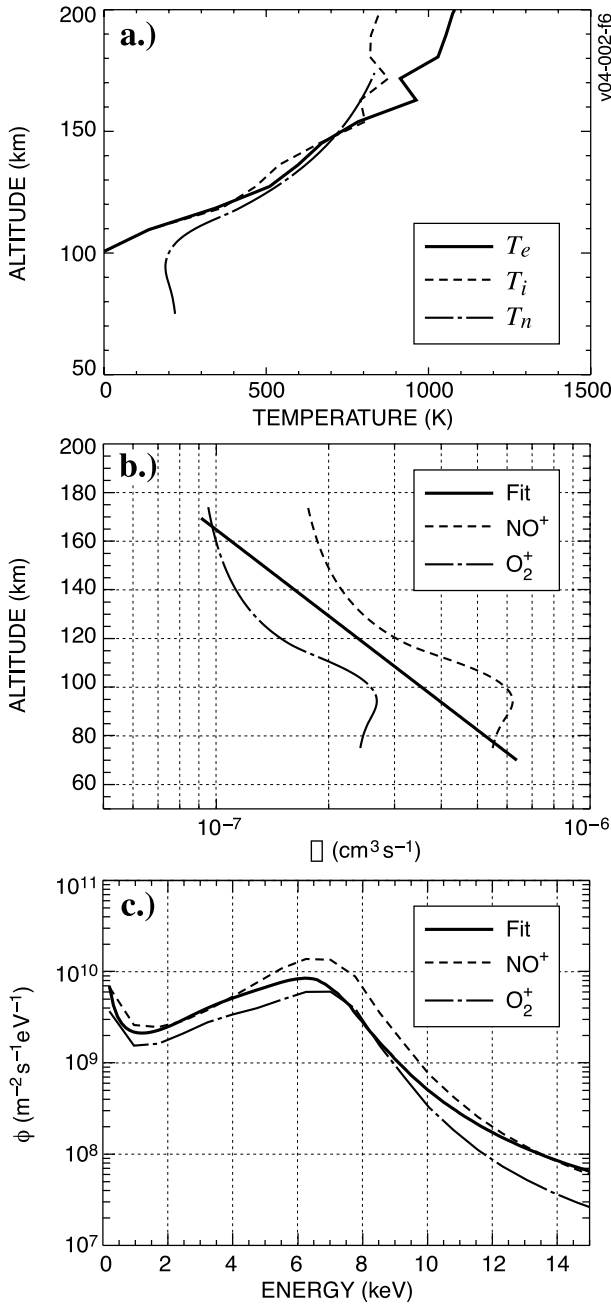


Figure 7. (a) Comparison of measured T_e and T_i with modelled T_n for 17 February 2001, 0230 UT. (b) Representative E region recombination coefficients α : all NO^+ (dashed), all O_2^+ (dot-dashed), average of published experimental results from *Vickrey et al.* [1982] (solid). (c) Result of ISR inversion on Figure 5c using the three assumed values for α .

wrong pitch angle distribution is applied to this profile in the inversion. The solid line is the known particle spectrum, the dashed line was computed using the unidirectional curve from Figure 1. As expected, the suprathermal peak in the recovered spectrum is erroneously spread out. The location of the peak in energy space is also significantly misrepresented. The recovered spectrum is reminiscent of the UNTANGLE and CARD results reported earlier in the literature [e.g., *Vondrak and Baron, 1975; Brekke et al., 1989*]. Although these authors did not state which pitch angle assumption was used, it is presumed that the unidirectional curve of *Rees* [1963] was used since this is the reference generally cited. As argued earlier, an isotropic distribution best represents the in situ observations. The isotropic Λ of Table 1 should be used for ISR inversion unless the actual pitch angle distribution is otherwise known.

3.2. Effective Recombination Coefficient

[38] Another source of uncertainty lies in the effective E region recombination coefficient α . The altitude dependence of α has been studied by several authors using rocket and ground-based measurements. Many of these results have been summarized by *Vickrey et al.* [1982], who proposed the following best fit parameterization:

$$\alpha_{fit} = 2.5 \times 10^{-12} e^{(-z/51.2)} \quad [\text{m}^3/\text{s}] \quad (25)$$

where z is in km. This altitude dependence is caused solely by altitude variability in the plasma and neutral temperatures. If the temperature profiles are known, we can use laboratory measurements of the principle E region reactants to more accurately model the recombination process. In particular, the principle ion species below 150 km are O_2^+ and NO^+ . Without knowing their mixing ratio, the measurements of *Walls and Dunn* [1974] place upper and lower bounds on α :

$$\alpha_{NO^+} = 4.2 \times 10^{-13} (300/T_n)^{0.85} \quad [\text{m}^3/\text{s}] \quad (26)$$

$$\alpha_{O_2^+} = 1.95 \times 10^{-13} (300/T_n)^{0.7} \quad (27)$$

[39] The plasma temperature can be directly sensed with the ISR. In the absence of anomalous local heating by strong electric fields [*Schlegel and St. Maurice, 1981*], T_i , T_e , and T_n are equal below 150 km. Figure 7a, for example, shows Sondrestrom ISR measurements of T_e (solid line) and T_i (dashed line) compared with T_n (dash-dot line) computed using the MSIS-90 model [*Hedin, 1991*]. Aside from the discrepancy at the lowest altitudes (below the range of applicability of ISR inversion), the modelled T_n agrees remarkably well with the measurements. Figure 7b compares α_{fit} with α_{NO^+} and $\alpha_{O_2^+}$, both computed using T_n from Figure 7a.

[40] Figure 7c shows how the choice of α affects the recovered spectrum. The solid line is a reproduction of Figure 5a, which was computed using α_{fit} . The other two curves are for α_{O^+} and α_{NO^+} . Despite the significant difference in the altitude dependencies for α_{fit} , α_{NO^+} and α_{O^+} , the recovered spectra are remarkably similar. For instance, E_0 (the location of the bump on tail) varies by less than 1 keV, while Φ (area under ϕ) varies by less than 10%. The significance of these finding will become evident in section 4, where we consider the time-dependent variability in the bulk plasma parameters.

[41] For the remainder of this paper we assume $\alpha = \alpha_{NO^+}$. This allows us to use the temperatures measured by the ISR in estimating α . The actual α probably lies between the outer extremes in Figure 7, but closer to the NO^+ curve. (Note that the composite curve labeled α_{fit} is not necessarily the most reliable choice since it was based on experimental methods with large uncertainties.)

3.3. Neutral Atmosphere Model

[42] The atmospheric mass density profile $\rho(z)$ controls the shape of the energy deposition profile. It is difficult to evaluate the reliability of ρ predicted by MSIS-90 directly. During active periods in the auroral zone, the ratio of atomic oxygen to molecular nitrogen in the 100 to 300 km altitude range decreases. This redistribution affects mass density profile. One possibility is to use proxy measurements, such as remote sensing measurements of the O/N_2 ratio [Hecht *et al.*, 2000], to constrain neutral composition. This may produce some improvement in the reliability of ISR inversion.

[43] However, one may also consider the relative timescales involved in evaluating the impact of the neutral atmosphere model. Changes in neutral composition occur over timescales that are long compared to timescales for auroral arc development. The error introduced into inverted spectra caused by inaccuracies in ρ will, thus, be largely of a systematic nature; we may still be able to discuss relative changes in bulk parameters of the recovered spectra even in the presence of large absolute uncertainties in ρ . A more careful consideration of neutral atmosphere uncertainties will be required if ISR inversion is to be used to study long the term statistical behavior of incident particle spectra.

3.4. Pulse Smearing

[44] Electron density sensed by ISR represents an average over a scattering volume which increases as range squared. If the pulse length is long compared to vertical gradient-scale lengths in the region under study, so-called pulse smearing can introduce significant artifacts into the inversion results. This is particularly important for the bottomside of the auroral E region, where pulse smearing can introduce an erroneous high-energy tail in the recovered energy spectrum. We

consider pulse smearing effects quantitatively in this section.

[45] Given a theoretical profile $n(r)$ sensed using a pulse of length r_P , the pulse-smear density at range r_0 becomes

$$n'(r_0) = \frac{r_0^2}{r_P} \int_{r_0 - \frac{r_P}{2}}^{r_0 + \frac{r_P}{2}} \frac{n(r)}{r^2} dr. \quad (28)$$

Figure 8a shows the density profile in Figure 5c sensed by a single pulse of length $r_P = 0, 2, 10, 24,$ and 48 km. The $r_P = 0$ and $r_P = 2$ km profiles are virtually indistinguishable. This means that for this incident electron spectrum, 2 km resolution is adequate to capture the induced altitude variability in the ionosphere. For larger values of r_P the peak altitude is biased upward, the layer broadens, and the peak density is decreased.

[46] The effect on the recovered electron spectrum is shown in Figure 8b. The original measured spectrum (i.e., $r_P = 0$) is shown by the dashed line. As expected, the spectrum is virtually unaltered for $r_P = 2$ km, but for larger values the location of the peak is significantly decreased, the width of the bump is narrowed, and the peak flux is increased. Another more subtle effect is the enhancement in the high-energy portion of the distribution; one must be cautious about interpreting ISR inversion results with respect to a Kappa distribution, or other distributions attempting to quantify deviations from Maxwellian at high energies. This problem is insidious because high-energy tails do, in fact, exist in space plasmas.

[47] Figure 8c shows the effect of pulse smearing on the bulk parameters. Plotted are the percentage change in Φ , Φ_E , and E_0 from the unbiased quantity as a function of pulse length. The estimated E_0 degrades almost linearly with pulse length: For a 320 μ s pulse (48 km pulse length) E_0 is underestimated by $\sim 60\%$. Interestingly though, Φ and Φ_E are less sensitive to pulse smearing. Φ retains over 80% of its value even using a 48 km pulse. This can be explained qualitatively by examining Figure 8b. As E_0 decreases $\phi(E_0)$ increases such that the area under ϕ remains roughly constant. This result means that long-pulse data can provide a reasonable estimate of net number flux even if E_0 cannot be reliably determined.

3.5. Effect of Deriving Density From Backscattered Power

[48] Accurate estimation of q using (18) requires that samples of n be recorded with temporal resolution similar to the average ion lifetime (~ 2 s for $n = 10^{12} \text{ m}^{-3}$), and with altitude resolution fine enough to resolve the steep bottomside gradients of the auroral E region (e.g., ~ 1 km). Because electron density is the only measured parameter entering the ISR inversion procedure, we may consider

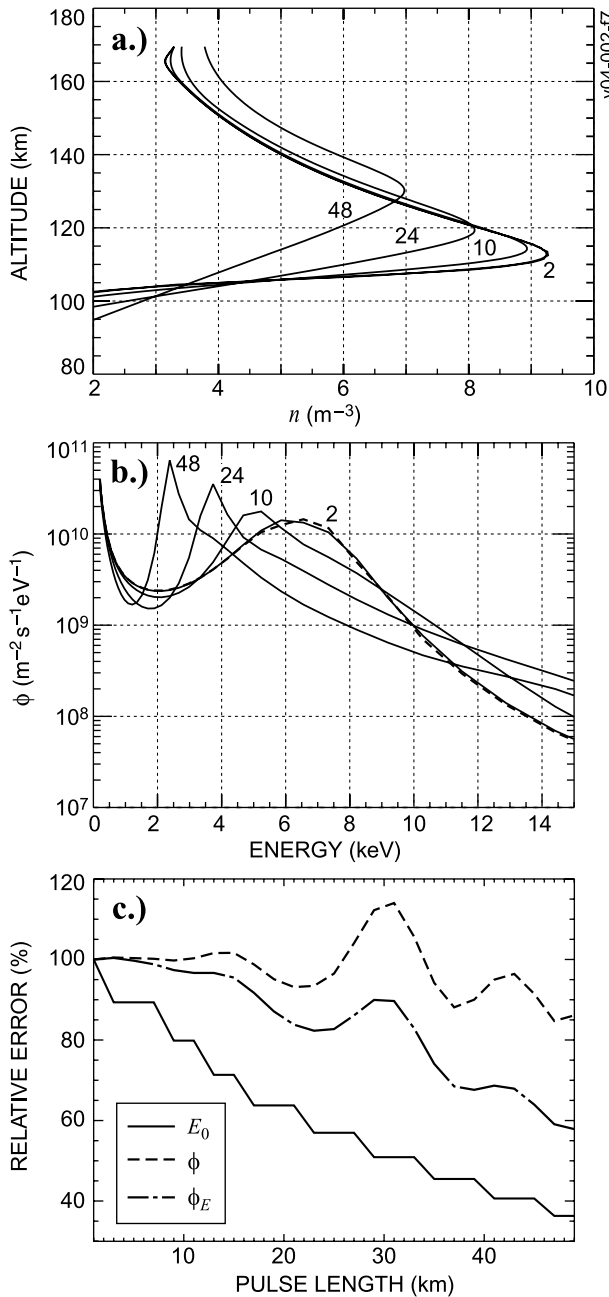


Figure 8. Effect of pulse smearing on ISR inversion: (a) $n(z)$ and (b) recovered $\phi(E)$ computed for various ISR pulse lengths (labels given in kilometers). (c) Percent error in E_0 , Φ_{E_s} , and Φ as a function of pulse length.

strategies that sacrifice fitting the ISR doppler spectrum in order to obtain increased spatial and temporal resolution. One such strategy uses the total backscattered power, corrected for range squared, as an estimate of n . Under

the Buneman approximation [e.g., *Evans 1969*], electron density is related to backscattered power by

$$n(z) = \frac{C_s z^2 P_r(z)}{P_t \tau} \left[\frac{(1 + \gamma^2 + T_e/T_i)(1 + \gamma^2)}{2} \right] \quad (29)$$

where P_t is the transmitted power, P_r is the backscattered power, τ is the pulse length, $\gamma = 2\pi D/\lambda$ is the Debye length correction, and C_s embodies the numerical constants of the radar system. In the F region, γ is typically 0.2, and T_r is typically between 1 and 4. In the auroral E region one can assume $T_e = T_i$ and $\gamma = 0$ in (29) such that

$$n_r(z) = \frac{C_s r^2 P_r(z)}{P_t \tau}. \quad (30)$$

This parameter is generally referred to as “raw n ”. Figure 9 compares n derived through spectral fitting (dashed line) with n_r (solid line) using a 20 s average of data recorded by the Sondrestrom ISR through an auroral arc. Clearly $n = n_r$ is a very reasonable assumption below 150 km (where the ISR inversion procedure is valid). The divergence of n and n_r at higher altitudes is caused by the divergence of T_e and T_i .

[49] Once n_r is established as a reliable representation of n , we may consider using pulse compression strategies to substantially increase the measurement resolution [*Gray and Farley, 1973*]. For auroral work at Sondrestrom,

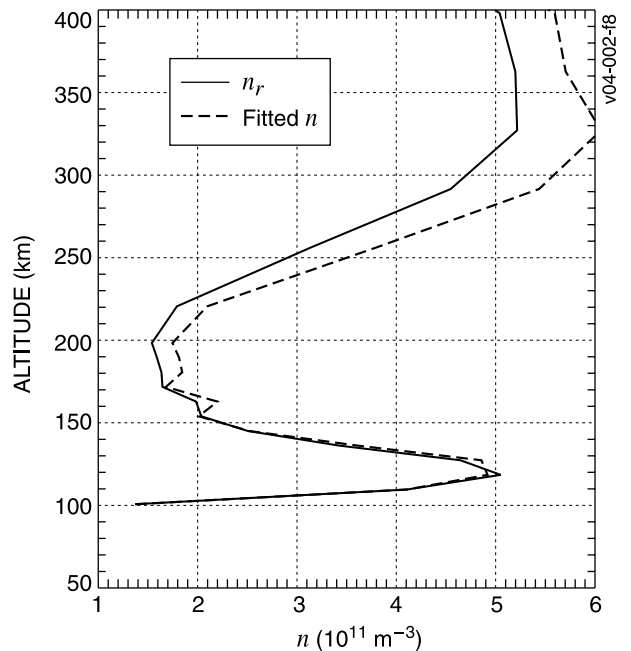


Figure 9. Comparison of n_r from equation (30) and fitted (temperature corrected) n for measurements of the auroral ionosphere over Sondrestrom, Greenland, on 17 February 2001, 0228.30 UT.

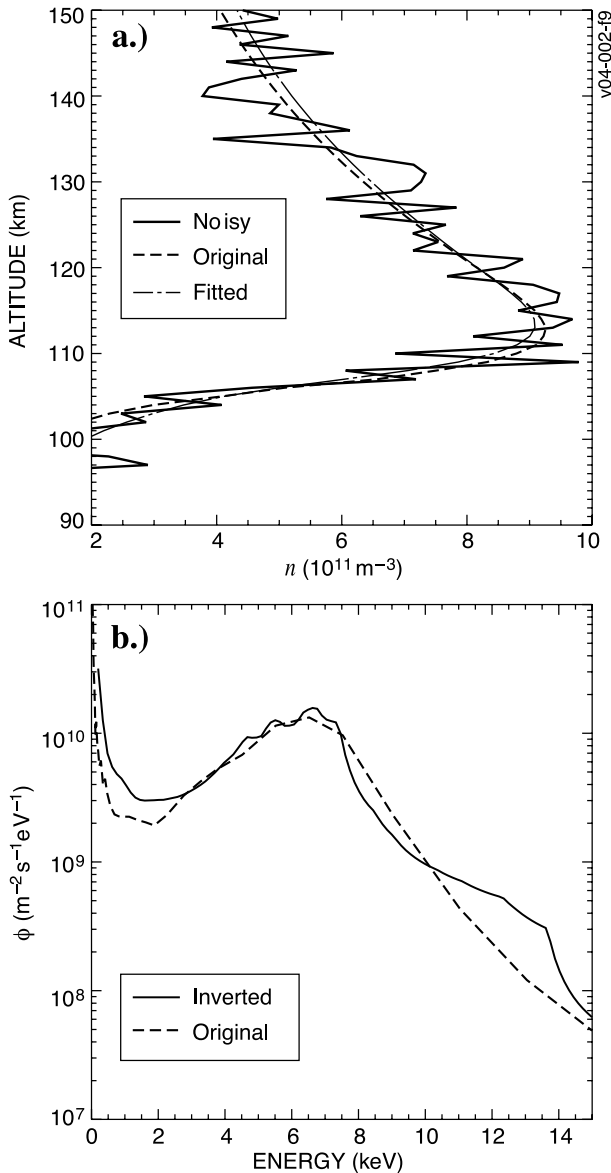


Figure 10. Effect of statistical noise on ISR inversion. (a) Original (dashed), noisy (solid) and fitted electron density profile after inversion of noisy data (dot-dashed). (b) Original ϕ (dashed) and estimated ϕ using noisy data (solid).

a 5-baud Barker code is commonly used. With this code, we have been able to acquire independent samples of the auroral E region at $1.2 \text{ s} \times 1 \text{ km}$ resolution with sufficient SNR for profile inversion (see section 4). Temporal resolution of 1.2 s is sufficiently small compared to the response time of the auroral E region to accurately capture the variability in the auroral source.

[50] There are cases where plasma wave heating can produce a significant discrepancy between T_e and T_i in the lower E region [Schlegel and St. Maurice, 1981], thus compromising the reliability of n_r . These conditions occur for very large electric fields ($>50 \text{ mV/m}$) typically near the edges of active auroral forms. To test for this condition, we typically transmit a single long pulse ($160 \mu\text{s}$) in addition to the coded pulse using a second transmit/receive channel. This provides an independent measure of T_e and T_i at 24 km resolution through the E region. This dual-channel observing mode has been described in some detail by Semeter and Doe [2002].

3.6. Statistical Uncertainties

[51] In section 5 we demonstrated the ability of the MEM inversion to handle the ill-conditioned nature of \mathbf{A} for ideal noiseless data. We now evaluate the robustness of the inversion procedure to statistical uncertainties. In Figure 10a, the test profile from Figure 5 has been corrupted by 0 mean, normally distributed, additive noise with standard deviation $\sigma = 1 \times 10^{11}/\text{m}^3$. This noise model has been chosen to qualitatively duplicate the worst case data we expect to encounter in our ISR profile inversion. Figure 10a may be compared, for instance, with actual Barker code measurements shown later.

[52] In Figures 10a and 10b, the dotted line shows the original density profile and electron spectrum, respectively. The solid line in Figure 10b shows the inversion results for the noisy profile. Although there is some deviation from the original spectrum, the recovered spectrum is a reasonable representation of the noiseless case. The dot-dashed line in Figure 10a shows the density profile fitted in the inversion. The low-pass filtering effect of the MEM inversion is evident; the fitted density profile deviates very little from the original noiseless density profile.

[53] Finally, one must be wary about smoothing noisy density profiles in an effort to obtain smoother results in the recovered spectra. One must not put too much emphasis on solution smoothness. A priori smoothing has essentially the same effect as pulse smearing. As shown in Figure 8, even a small amount of data smoothing can introduce significant errors into the recovered spectra.

4. Time-Dependent ISR Inversion

[54] We now present an example of time-dependent ISR inversion using measurements of an auroral surge over Sondrestrom on 17 February 2001. Figure 11a shows plasma density as a function of altitude and time for a 2-min period during which an auroral surge developed and faded in zenith. The data were recorded using the Barker coded pulse previously described and the plotted parameter is n_r from equation (30).

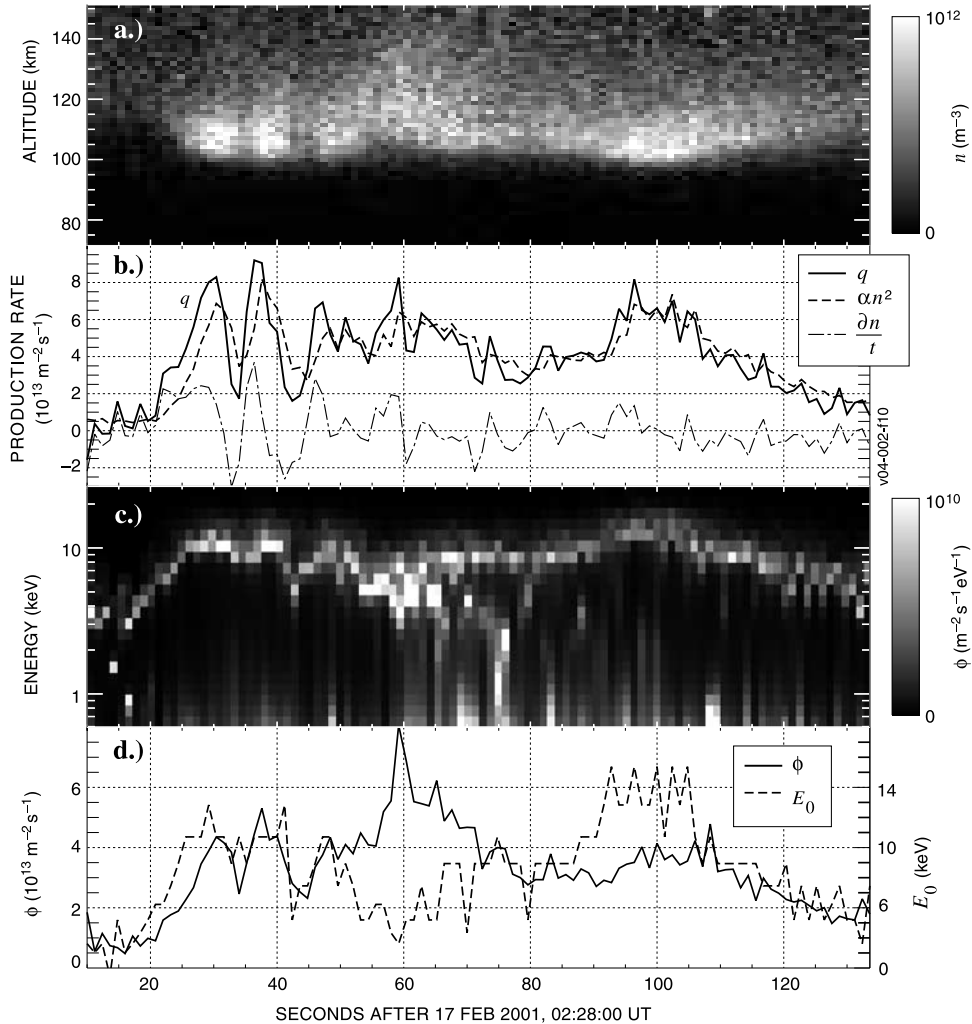


Figure 11. Analysis of auroral surge event on 17 February 2001: (a) $n_r(z, t)$ and (b) height-integrated ion production rate (solid line) compared with component terms from equation (18). (c) Recovered $\phi(K, t)$. (d) Bulk parameters Φ and E_0 computed from the recovered spectra.

[55] Our first task is to compute a reliable estimate of q from these data. It is insightful to compare the time-dependent and steady state terms of (18) computed from these data. Figure 11b compares the height-integrated quantities $\int Dn/Dtdz$ (dash-dot line), $\int \alpha n^2 dz$ (dashed line), and their sum $\int q dz$ (solid line). In the interval 0228.20–0228.30 UT, when the density is initially increasing, measurements from a collocated auroral camera tell us that the arc is stationary within the zenith-looking radar beam as it gains in luminosity. Therefore in this interval it is appropriate to include Dn/Dt in the calculation of q . Ignoring this term would result in a significant misrepresentation of q in this interval. By contrast, images recorded during the next increase in n (0228.30–0228.40 UT) show that Dn/Dt is

caused by an advecting arc. In this interval we let $q = \alpha n^2$. For the remainder of the event, Figure 11b shows that Dn/Dt term is small compared to αn^2 .

[56] Figure 12 compares the three terms of (18) as a function of altitude for these two time periods, i.e., when q is increasing (upper panel) and when q is decreasing (lower panel). The camera data suggest that $Dn/Dt = dn/dt$ in the upper panel, but that $Dn/Dt = v \cdot \nabla n$ in the lower panel. In early applications of ISR profile inversion, the dn/dt term was ignored. Figures 11b and 12 highlight the danger of either falsely assuming steady state or falsely assuming no advection.

[57] Figure 11c shows the differential number flux spectrum ϕ versus altitude and time estimated via ISR inversion. The plot is reminiscent of satellite measure-

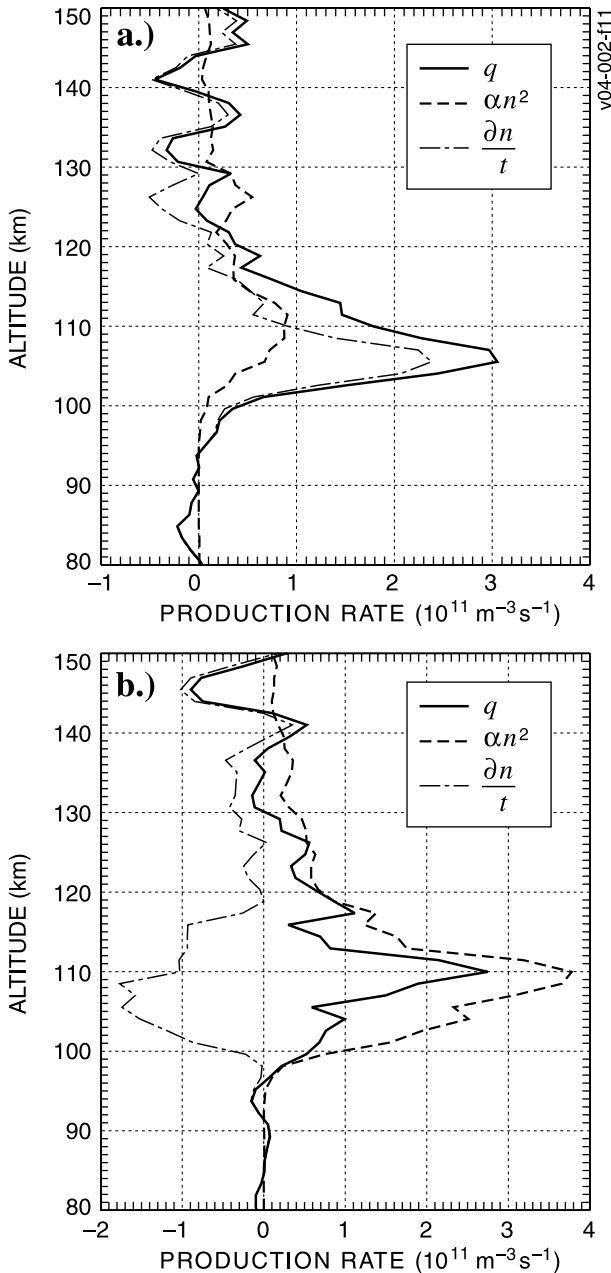


Figure 12. Comparison of q computed from equation (18) with the two component terms on the right-hand side for increasing (upper panel) and decreasing (lower panel) auroral ionization. In the upper panel, Dn/Dt is caused by a change in the auroral source, in the lower panel Dn/Dt is caused by advection of an auroral flux tube.

ments of inverted-V aurora [e.g., *McFadden et al.* 1999]. However, the present result is of a rather different nature. Satellites traverse a 10 km auroral form in less than 1 s. Satellite measurements are thus of a “snapshot” nature. Here we are monitoring variability in the accelerated distribution at a fixed local time. The results contain both spatial variability (motion of auroral flux tubes through the beam) and temporal variability (changes in precipitation on a flux tube). As we have just shown, this ambiguity can be addressed using ground-based imagery. For instance, we know that the increase in E_0 and Φ in the 0228.20–0228.30 UT interval reflects the temporal development of the auroral acceleration region.

[58] Although we do not have independent verification of the results of Figure 11, we have shown in section 5 that the estimation of bulk parameters is robust to the level of statistical uncertainties in these data. For instance, we may compare measured and fitted densities, similar to Figure 10. Figure 13a (solid line) shows the measured electron density profile at 0229.40 UT, a period when $dn/dt \sim 0$. The fitted density is shown by the dashed line and the recovered spectrum is shown in Figure 13b. As in Figure 10, the inversion produced a smooth fit to the noisy data.

[59] Last, Figure 11d shows E_0 and Φ computed from the recovered spectra using (21) and (23), respectively. There are three noteworthy periods to consider. First, between 20 s and 30 s note that the rise in Φ lags behind the rise in E_0 . Optical measurements show that the aurora is brightening in place during this interval, with little apparent motion of the source. The combined optical and radar diagnostics suggest that the behavior of the bulk parameters reflects a characteristic of the acceleration region itself; namely, that the formation of the aggregate parallel potential drop on this flux tube leads the increase in flux through it.

[60] A second interesting period is between 50 s and 70 s, where Φ and E_0 become anticorrelated. During this period the optical record shows faint fast moving structures in the zenith. This same behavior was reported by *Semeter et al.* [2001b] in a region where the precipitation was dominated by suprathermal electron bursts. It is possible that an anticorrelation in Φ and E_0 indicates a transition to a regime of wave accelerated electrons.

[61] Finally, between 85 s and 95 s the increase in E_0 is not accompanied by any significant change in Φ . The optical measurements show that the auroral forms are re-energizing at this time. The inversion results, again, suggest that the development of a parallel potential drop that leads the electron flux through it.

5. Summary and Conclusions

[62] Polar orbiting satellites provide detailed spatial pictures of the electron distribution functions responsible

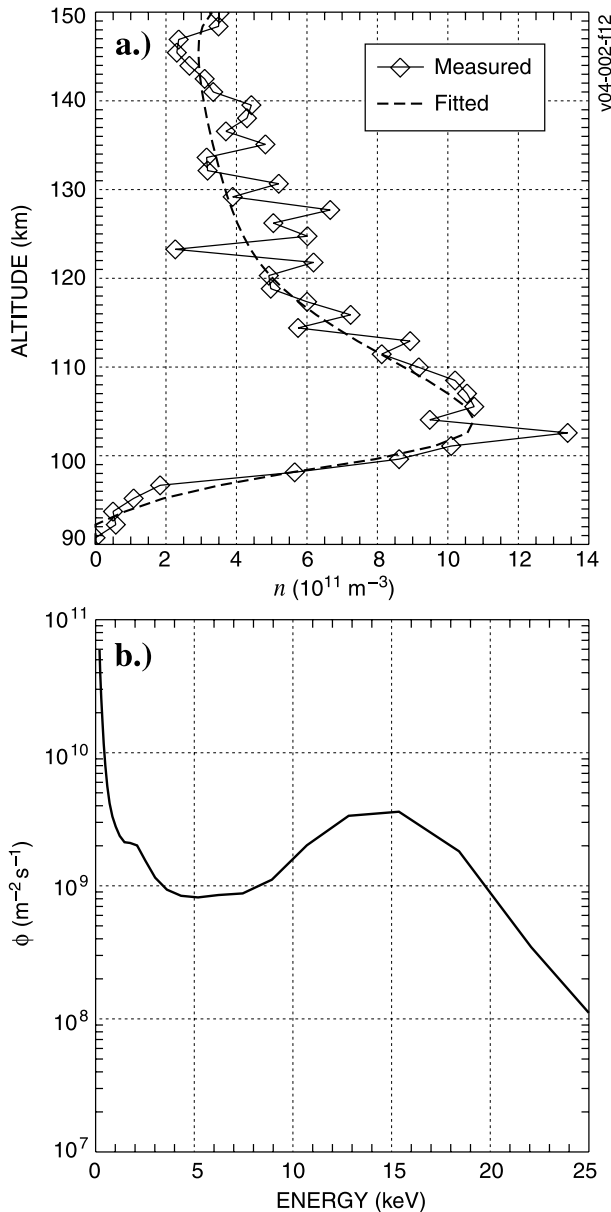


Figure 13. ISR inversion on 17 February 2001, 0229.40 UT: (a) measured and fitted n and (b) recovered ϕ .

for the aurora. But however detailed these measurements become, they cannot directly elucidate the time-dependent physics governing the development of the auroral acceleration region. This problem requires measurements in the frame of reference of an auroral flux tube over timescales of 10s of seconds. The technique presented herein provides this missing perspective, and is especially effective when used in combination with high-resolution optical

measurements. The challenge is to interpret inversion results with a proper understanding the technique’s limitations. By evaluating the robustness of the ISR inversion procedure to various measurement and model uncertainties, we have made a critical step toward this goal.

[63] We have derived a forward model following the approach of *Rees* [1963]. By comparison with Rees, our results have a less pronounced discontinuity at $s/R = 0$ due to better accounting of the backscattered energy. We then described an inversion procedure based on the maximum entropy method (MEM). We showed that MEM is well suited for the attributes of this model kernel. The solution is quite robust to the initial guess and input parameter choices (i.e., relaxation parameter, distribution and number of energy bins).

[64] We then evaluated the robustness of the procedure to six major sources of uncertainty: (1) the pitch angle distribution, (2) the recombination coefficient, (3) the neutral atmosphere model, (4) radar pulse smearing effects, (5) statistical errors in n , and (6) the use of range-corrected power as a measure of n . The first three are related to the forward model; the last three are related to measurements. The procedure is particularly sensitive to the assumed pitch angle distribution. However, in situ measurements have shown that the majority of the energy flux is generally carried by the high-energy (>1 keV) isotropic distribution. We argue that the “isotropic” Λ , tabulated in Table 1, best represents the auroral source during active periods, and that errors associated with this assumption are minimal.

[65] We evaluated three plausible models of the height-dependent recombination coefficient. While the shape of the recovered spectrum depends somewhat on the choice of α , the bulk parameters Φ and E_0 do not. We adopted the NO^+ coefficient derived by *Walls and Dunn* [1974] since it allows one to incorporate the ISR measured temperature dependence.

[66] The neutral atmosphere model affects ISR inversion through the mass density ρ . Errors in ρ may introduce a systematic bias to the results, but the relative change in bulk parameters should be preserved. This is because the time constant for changes in atmospheric mass density is long compared to timescales we are interested in for auroral formation.

[67] Finally, we have demonstrated that measurements uncertainties do not impose critical limitations in this analysis. Pulse smearing effects are mitigated through the use of pulse compression techniques, which can provide independent samples of n at $1 \text{ s} \times 1 \text{ km}$ resolution for the Sondrestrom radar. We can thus capture both the steep altitude gradients and temporal variability in the ionization response. Although these samples will be noisy, MEM inversion produces intrinsically smooth results.

[68] The time-dependent analysis of Sondrestrom measurements summarized in Figure 11 demonstrates

the potential of the ISR inversion technique for investigating the development of the auroral acceleration region. Figure 11b is reminiscent of in situ measurements of so-called “inverted-V” auroral fluxes observed by polar orbiting satellites and rockets [e.g., *McFadden et al.* 1999]. However, the variability here is observed from a geostationary reference frame, such that the results contain a mixture of spatial and temporal variability. Another advantage of ground-based analysis is that collocated cameras can be used to address this spatial-temporal ambiguity.

Appendix A: Maximum Entropy Solution

[69] To compute the regularized inverse of \mathbf{A} , we use the Maximum Entropy algorithm of *De Pierro* [1991]. This algorithm maximizes the negative Berg entropy $-\ln\phi$, subject to the side constraint that the residual noise distribution $\mathbf{q} - \mathbf{A}\phi$ matches the a priori noise distribution. A variant of this algorithm was used by *Semeter et al.* [1999] in the context of ground-based tomography of airglow and auroral emissions. The iteration steps are as follows:

$$\phi_j^{k+1} = \frac{\phi_j^k}{1 - \phi_j^k \sum_{i=1}^I w_i c_i^k A_{ij}} \quad (\text{A1})$$

$$c_i^k = \beta_k \left(1 - \frac{\langle \mathbf{A}_i, \phi^k \rangle}{q_i} \right) t^k \quad (\text{A2})$$

$$t_i^k = \min_j \left\{ \frac{1}{A_{ij} \phi_j^k} \mid A_{ij} \neq 0 \right\}, \quad (\text{A3})$$

[70] The relaxation parameter β_k controls the degree to which the solution is allowed to change in each step. We have found that a constant value of $\beta = 20$ works well for the ISR inversion problem. The ω_i 's are positive real numbers such that

$$\sum_{i=1}^{N_q} \omega_i = 1 \quad (\text{A4})$$

with N_q the number of elements of q .

[71] Convergence is monitored through the waited residual norm (equivalent to the χ^2 function):

$$\chi^2 = \sum_{N_q} \frac{|\mathbf{q} - \mathbf{A}\phi|^2}{\sigma_q^2} \quad (\text{A5})$$

where σ_q^2 is the estimated noise variance. The noise variance (equivalent to noise power) is sampled and stored for each pulse. Using this information, iterations

can proceed until $\chi^2 = 1$. This generally requires between 50 and 200 iteration steps. On a Pentium-3 laptop, each profile requires ~ 4 s to invert.

[72] **Acknowledgments.** The authors wish to thank E. M. Blixt, J. P. Thayer, C. J. Heinselman, and R. A. Doe for helpful discussions. We also wish to thank J. Jorgensen and the Sondrestrom site crew for campaign support, and M. McCready for data preparation. This work was supported by the National Science Foundation under grants ATM-0302672 and ATM-9317167.

References

- Barrett, J., and P. Hays (1976), Spatial distribution of energy deposited in nitrogen by electrons, *J. Chem. Phys.*, *64*, 743–750.
- Brekke, A., C. Hall, and T. Hansen (1989), Auroral ionospheric conductances during disturbed conditions, *Ann. Geophys.*, *7*, 269–280.
- Burns, C., W. Howarth, and J. Hargreaves (1990), High-resolution incoherent scatter radar measurements during electron precipitation events, *J. Atmos. Terr. Phys.*, *52*, 205–218.
- Censor, Y. (1981), Row-action methods for huge and sparse systems and their applications, *SIAM Rev.*, *23*, 444–466.
- Christensen, A. B., L. R. Lyons, J. H. Hecht, G. G. Sivjee, and R. R. Meier (1987), Magnetic field-aligned electric field acceleration and the characteristics of the optical aurora, *J. Geophys. Res.*, *92*, 6163–6167.
- Cohn, A., and G. Caledonia (1970), Spatial distribution of the fluorescent radiation emission caused by an electron beam, *J. Appl. Phys.*, *41*, 3767–3775.
- Dalgarno, A. (1962), Range and energy loss, in *Atomic and Molecular Processes*, edited by D. Bates, pp. 622–651, Elsevier, New York.
- De Pierro, A. (1991), Multiplicative iterative methods in computed tomography, in *Mathematical Methods in Tomography*, edited by G. Herman, A. Louis, and F. Natterer, pp. 1441–1450, Springer, New York.
- Evans, J. (1969), Theory and practice of ionospheric study by Thomson scatter radar, *Proc. IEEE*, *57*, 496–530.
- Fano, U. (1946), On the theory of ionization yield of radiations in different substances, *Phys. Rev.*, *70*, 44–52.
- Frey, S., H. Frey, D. Carr, O. Bauer, and G. Haerendel (1996), Auroral emission profiles extracted from three-dimensionally reconstructed arcs, *J. Geophys. Res.*, *101*, 21,731–21,742.
- Gray, R., and D. Farley (1973), Theory of incoherent-scatter measurements using compressed pulses, *Radio Sci.*, *8*, 123–131.
- Grün, A., and C. Barth (1957), Lumineszenz-photometrische Messungen der Energieabsorption in Strahlungsfeld von Elektronquellen: Eindimensionaler Fall in Luft, *Z. Naturf.*, *12a*, 89.
- Gull, S., and G. Daniell (1978), Image reconstruction from incomplete and noisy data, *Nature*, *272*, 686–690.

- Gustavsson, B. (1998), Tomographic inversion for ALIS noise and resolution, *J. Geophys. Res.*, *103*, 26,621–26,632.
- Hecht, J., D. J. Strickland, A. B. Christensen, D. Kayser, and R. Walterscheid (1991), Lower thermospheric composition changes derived from optical and radar data taken at Sondre Stromfjord during the great magnetic storm of February 1986, *J. Geophys. Res.*, *96*, 5757–5776.
- Hecht, J., D. L. McKenzie, A. B. Christensen, D. J. Strickland, J. P. Thayer, and J. Watermann (2000), Simultaneous observation of lower thermospheric composition change during moderate auroral activity from Kangerlussuaq and Narsarsuaq Greenland, *J. Geophys. Res.*, *105*, 27,109–27,118.
- Hedin, A. (1991), Extension of the MSIS thermosphere model into the middle and lower atmosphere, *J. Geophys. Res.*, *96*, 1159–1172.
- Kamalabadi, F., et al. (2002), Tomographic studies of aeronomical phenomena using radio and UV techniques, *J. Atmos. Sol. Terr. Phys.*, *64*, 1573–1580.
- Kirkwood, S. (1988), SPECTRUM—A computer algorithm to derive the flux-energy spectrum of precipitating particles from EISCAT electron density profiles, *IRF Tech. Rep. 034*, Swed. Inst. of Space Phys., Kiruna, Sweden.
- Kirkwood, S., and L. Eliasson (1990a), Energetic particle precipitation in the substorm growth phase measured by EISCAT and Viking, *J. Geophys. Res.*, *95*, 6025–6037.
- Kirkwood, S., and L. Eliasson (1990b), Energetic particle precipitation in the substorm growth phase measured by EISCAT and Viking, *J. Geophys. Res.*, *95*, 6025–6037.
- Lummerzheim, D., and J. Liliensten (1994), Electron transport and energy degradation in the ionosphere: Evaluation of the numerical solution, comparison with laboratory experiments and auroral observations, *Ann. Geophys.*, *12*, 1039–1051.
- Lyons, L., R. Lundin, and D. Evans (1979), An observed relation between magnetic field aligned electric fields and downward electron energy fluxes in the vicinity of auroral forms, *J. Geophys. Res.*, *84*, 457–461.
- McFadden, J., C. Carlson, and R. Ergun (1999), Microstructure of the auroral acceleration region observed by FAST, *J. Geophys. Res.*, *104*, 14,453–14,480.
- Meier, R., D. Strickland, J. Hecht, and A. Christensen (1989), Deducing composition and incident electron spectra from ground-based auroral optical measurements: A study of auroral red line processes, *J. Geophys. Res.*, *94*, 13,541–13,552.
- Moen, J., A. Brekke, and C. Hall (1990), An attempt to derive electron energy spectra for auroral daytime precipitation events, *J. Atmos. Terr. Phys.*, *52*, 459–471.
- Osepian, A., and S. Kirkwood (1996), High-energy electron fluxes derived from EISCAT electron density profiles, *J. Atmos. Terr. Phys.*, *58*, 479–487.
- Rees, M. (1963), Auroral ionization and excitation by incident energetic electrons, *Planet. Space Sci.*, *11*, 1209–1218.
- Rees, M. (1989), *Physics and Chemistry of the Upper Atmosphere*, Cambridge Univ. Press, New York.
- Rees, M., and D. Luckey (1974), Auroral electron energy derived from ratio of spectroscopic emissions, 1, model computations, *J. Geophys. Res.*, *79*, 5181–5186.
- Schlegel, K., and J.-P. St. Maurice (1981), Anomalous heating of the polar E region by unstable plasma waves: 1. Observations, *J. Geophys. Res.*, *86*, 1042–1048.
- Semeter, J., and R. Doe (2002), On the proper interpretation of ionospheric conductance estimated through satellite photometry, *J. Geophys. Res.*, *107*(A8), 1200, doi:10.1029/2001JA009101.
- Semeter, J., M. Mendillo, and J. Baumgardner (1999), Multi-spectral tomographic imaging of the midlatitude aurora, *J. Geophys. Res.*, *104*, 24,565–24,585.
- Semeter, J., D. Lummerzheim, and G. Haerendel (2001a), Simultaneous multispectral imaging of the discrete aurora, *J. Atmos. Sol. Terr. Phys.*, *63*, 1981–1992.
- Semeter, J., J. Vogt, G. Haerendel, K. Lynch, and R. Arnoldy (2001b), Persistent quasiperiodic precipitation of suprathermal ambient electrons in decaying auroral arcs, *J. Geophys. Res.*, *106*, 12,863–12,874.
- Sharif, B., and F. Kamalabadi (2004), Complexity regularized parametric estimation for radar deconvolution, paper presented at International Symposium on Information Theory, Inst. of Electr. and Electron. Eng., New York.
- Strickland, D., R. Meier, J. Hecht, and A. Christensen (1989), Deducing composition and incident electron spectra from ground-based auroral optical measurements: Theory and results, *J. Geophys. Res.*, *94*, 13,527–13,539.
- Vallance-Jones, A. (1974), *Aurora*, Springer, New York.
- Vickey, J., R. Vondrack, and S. Matthews (1982), Energy deposition by precipitating particles and joule dissipation in the auroral ionosphere, *J. Geophys. Res.*, *87*, 5184–5196.
- Vondrak, R., and M. Baron (1975), A method of obtaining the energy distribution of auroral electrons from incoherent scatter radar measurements, in *Radar Probing of the Auroral Plasma*, edited by A. Brekke, pp. 315–330, Univ. Etsforlaget, Oslo.
- Walls, F., and G. Dunn (1974), Measurements of total cross sections for electron recombination with NO^+ and O_2^+ using ion storage techniques, *J. Geophys. Res.*, *79*, 1911–1915.

F. Kamalabadi, Department of Electrical and Computer Engineering, University of Illinois at Urbana-Champaign, 1308 West Main Urbana, IL 61801, USA. (farzadk@uiuc.edu)

J. Semeter, Department of Electrical and Computer Engineering and Center for Space Physics, Boston University, 8 Saint Mary's Street, Boston, MA 02215, USA. (jls@bu.edu)